



**CHALMERS**  
UNIVERSITY OF TECHNOLOGY

## **Nanostructured Transition Metal Dichalcogenide Multilayers for Advanced Nanophotonics**

Downloaded from: <https://research.chalmers.se>, 2024-04-19 15:10 UTC

Citation for the original published paper (version of record):

Munkhbat, B., Küçüköz, B., Baranov, D. et al (2023). Nanostructured Transition Metal Dichalcogenide Multilayers for Advanced Nanophotonics. *Laser and Photonics Reviews*, 17(1).  
<http://dx.doi.org/10.1002/lpor.202200057>

N.B. When citing this work, cite the original published paper.

# Nanostructured Transition Metal Dichalcogenide Multilayers for Advanced Nanophotonics

Battulga Munkhbat, Betül Küçüköz, Denis G. Baranov, Tomasz J. Antosiewicz, and Timur O. Shegai\*

Transition metal dichalcogenides (TMDs) attract significant attention due to their exceptional optical, excitonic, mechanical, and electronic properties. Nanostructured multilayer TMDs were recently shown to be highly promising for nanophotonic applications, as motivated by their exceptionally high refractive indices and optical anisotropy. Here, this vision is extended to more sophisticated structures, such as periodic arrays of nanodisks and nanoholes with ultra sharp walls, as well as proof-of-concept all-TMD waveguides and resonators. Specific focus is given to various advanced nanofabrication strategies, including careful selection of resists for electron beam lithography and etching methods, especially for non-conductiven but relevant for nanophotonic applications substrates, such as SiO<sub>2</sub>. The specific materials studied here include semiconducting WS<sub>2</sub>, in-plane anisotropic ReS<sub>2</sub>, and metallic TaSe<sub>2</sub>, TaS<sub>2</sub>, and NbSe<sub>2</sub>. The resulting nanostructures can potentially impact several nanophotonic and optoelectronic areas, including high-index nanophotonics, plasmonics and on-chip optical circuits. The knowledge of TMD material-dependent nanofabrication parameters developed here will help broaden the scope of future applications of all-TMD nanophotonics.

## 1. Introduction

Nanostructuring is one of the most attractive and facile ways to enrich material properties. In layered transition metal dichalcogenide (TMD) materials, nanostructuring can be readily introduced through exfoliation. This approach is now routinely exploited down to the monolayer limit and the resulting TMD monolayers exhibit remarkable physical and chemical properties. For instance, the recent interest in 2D semiconductors is largely motivated by the discovery of a direct bandgap in monolayer MoS<sub>2</sub>.<sup>[1,2]</sup> Furthermore, TMD monolayers can be assembled into van der Waals (vdW) heterostructures, which enrich material properties through formation of Moiré superlattices.<sup>[3]</sup> The possible confinement of TMD materials, however, is not limited to the out-of-plane direction and thus to monolayer physics.

A straightforward alternative is in-plane confinement, which can be achieved through various kinds of structural etching and can be realized in both TMD mono- and multilayers.<sup>[4–9]</sup> Such nanostructuring can introduce an additional degree of freedom in tailoring physical and chemical properties of TMD materials on various scales, including edge physics and nanophotonics.


Applying the nanopatterning approach to TMD multilayers can bear interest since multilayers possess several attractive optical, electronic, and mechanical<sup>[10]</sup> properties, which can be potentially enhanced and/or enriched through nanofabrication. Optical properties of TMDs are determined by their atomic lattice and the corresponding electron band structure. Many TMDs feature excitonic resonances in the visible and near infrared range that possess high oscillator strength and are stable both in mono- and multi-layer materials at room temperature. Owing to Kramers–Kronig relations, these excitonic transitions endow TMDs with relatively high refractive indices ( $n \approx 4$ ) at energies just below the respective transition.<sup>[5,11–13]</sup> At even lower energies (longer wavelengths) where the refractive index remains large but the material's absorption coefficient quickly vanishes, these materials can be exploited for lossless waveguiding and light confinement.<sup>[12–19]</sup> Furthermore, all TMDs are naturally anisotropic due to their vdW nature, endowing them with an inherent optical uniaxial permittivity with  $\epsilon_{xx} = \epsilon_{yy} \neq \epsilon_{zz}$ .<sup>[8,13,14,17,20]</sup>

B. Munkhbat, B. Küçüköz, D. G. Baranov, T. J. Antosiewicz, T. O. Shegai  
Department of Physics  
Chalmers University of Technology  
Göteborg 412 96, Sweden  
E-mail: timurs@chalmers.se

D. G. Baranov  
Center for Photonics and 2D Materials  
Moscow Institute of Physics and Technology  
Dolgoprudny 141700, Russia

D. G. Baranov  
Russian Quantum Center  
Skolkovo Innovation Center  
Moscow, Moscow 121205, Russia

T. J. Antosiewicz  
Faculty of Physics  
University of Warsaw  
Pasteura 5, Warsaw 02-093, Poland

 The ORCID identification number(s) for the author(s) of this article can be found under <https://doi.org/10.1002/lpor.202200057>

© 2022 The Authors. Laser & Photonics Reviews published by Wiley-VCH GmbH. This is an open access article under the terms of the Creative Commons Attribution-NonCommercial License, which permits use, distribution and reproduction in any medium, provided the original work is properly cited and is not used for commercial purposes.

DOI: 10.1002/lpor.202200057

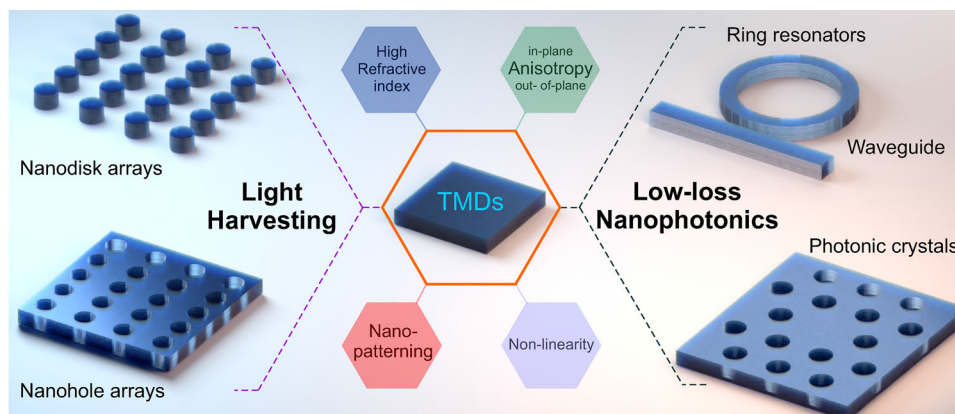


**Figure 1.** Roadmap for all-TMD nanophotonics. Exploring nanostructured TMDs for future applications in light absorption (left), and low-loss nanophotonics (right). This vision is based on remarkable properties of multilayer TMDs, such as high refractive index, optical anisotropy, and optical nonlinearity. The purpose of this work is to demonstrate improvement in optical response of TMDs through nanostructuring.

In certain materials (e.g., in  $\text{ReS}_2$ ) a distortion of the planar hexagonal lattice leads to biaxial anisotropy with different values of the in-plane permittivity tensor elements, that is,  $\epsilon_{xx} \neq \epsilon_{yy}$  and both being different from the out-of-plane  $\epsilon_{zz}$ .<sup>[21–23]</sup> Nonlinear optical properties of multilayer TMDs, such as second-harmonic generation (SHG), also attract research attention.<sup>[6,24,25]</sup> Here, bulk materials characterized by broken inversion symmetry, such as multilayer  $\text{ReS}_2$  or hBN, play an important role.<sup>[26,27]</sup>

Nanostructured multilayer TMDs are thus promising candidates for future nanophotonic and optoelectronic applications.<sup>[18,28]</sup> Although several examples of TMD nanostructuring have already been reported in the literature,<sup>[4–9,24,25,29–32]</sup> detailed investigations of nanopatterned TMDs as well as advanced ways of their nanofabrication are just starting to appear. Thus, a material-oriented study focusing on advanced nanofabrication procedures for TMD multilayers and demonstrating a potential of all-TMD nanophotonics is of high contemporary interest. In this regard, careful testing and optimization of the fabrication procedures, applicable not only for semiconducting but also for metallic TMDs, and tested on various challenging to work with substrates, are of particular interest. This fabrication-oriented progress, together with theoretical efforts<sup>[16,18,19]</sup> and knowledge of basic optical constants,<sup>[13]</sup> is essential for the development of all-TMD nanophotonics.

In this paper, we present fabrication of TMD nanostructures confined in one, two, or all three dimensions, and experimentally measure and analyze some of their optical properties both in the linear and non-linear regimes. The key novelty aspect of our work is careful and tailored optimization of nanofabrication processes for various kinds of TMDs developed for use on practically challenging substrates, such as, thin non-conductive  $\text{SiO}_2$ . The latter is of particular importance for optical microscopy and nanophotonics applications. Using bulk TMD crystals as a starting point, we fabricated series of unique nanophotonic structures, including nanodisk and nanohole arrays, proof-of-principle waveguides, microring resonators, photonic crystal cavities, as well as individual nanodisks and nanorods. In the linear regime, nanopatterned  $\text{WS}_2$  arrays exhibit various resonant features including Mie-type resonances and diffractive modes observed using reflection optical spectroscopy and dark-field mi-

croscopy. In the non-linear regime, TMD arrays exhibit selective enhancement of SHG signal. Nanopatterned  $\text{WS}_2$  structures also hold promise for optical waveguiding, for example, bus-coupled microring structures, and for light localization in photonic crystal cavities as demonstrated herein through fabrication of model nanophotonic structures and numerical modeling. Nanopatterning is feasible also for in-plane anisotropic TMDs such as  $\text{ReS}_2$  as well as uniaxial metallic TMDs represented here by  $\text{TaS}_2$ ,  $\text{TaSe}_2$  and  $\text{NbSe}_2$ . An example of the former includes hexagonal nanodisk arrays, while for the latter we demonstrated accurate fabrication of single-element and dimer nanoantennas. The results reported here broaden the scope of potential applications of TMD materials in nanophotonics and optoelectronics.

**Figure 1** conceptualizes the approach to all-TMD nanophotonics that we follow in this study. TMD materials combine a spectral region of high absorption associated with their excitonic resonances, and a low optical loss region at energies below the A-exciton resonance.<sup>[11]</sup> These two regimes determine two different application areas where nanostructured TMDs can be exploited: i) light absorption, and ii) light confinement and guiding, correspondingly. Accordingly, we split our investigation of nanostructured TMDs into two parts. In the first, we demonstrate the capabilities of nanostructured TMDs for light harvesting purposes by utilizing the absorptive behavior of TMDs in the visible frequency range. In the second part, we present and discuss the capabilities of nanostructured TMDs for light confinement and guiding in the long-wavelength part of the spectrum in which these materials exhibit low losses. In the following, we examine different types of nanostructures suited for both objectives presented in this study, discuss methods with which to fabricate them,<sup>[5,8,9]</sup> characterize their optical response using various spectroscopic methods, and provide numerical simulation results.

## 2. TMD Nanostructures for Light Absorption

We begin our discussion by examining periodic arrays of TMD nanodisks and nanoholes, whose usefulness is based on the high refractive index of TMDs.<sup>[5,11]</sup> These systems possess optical resonances associated with the modes of individual elements, such

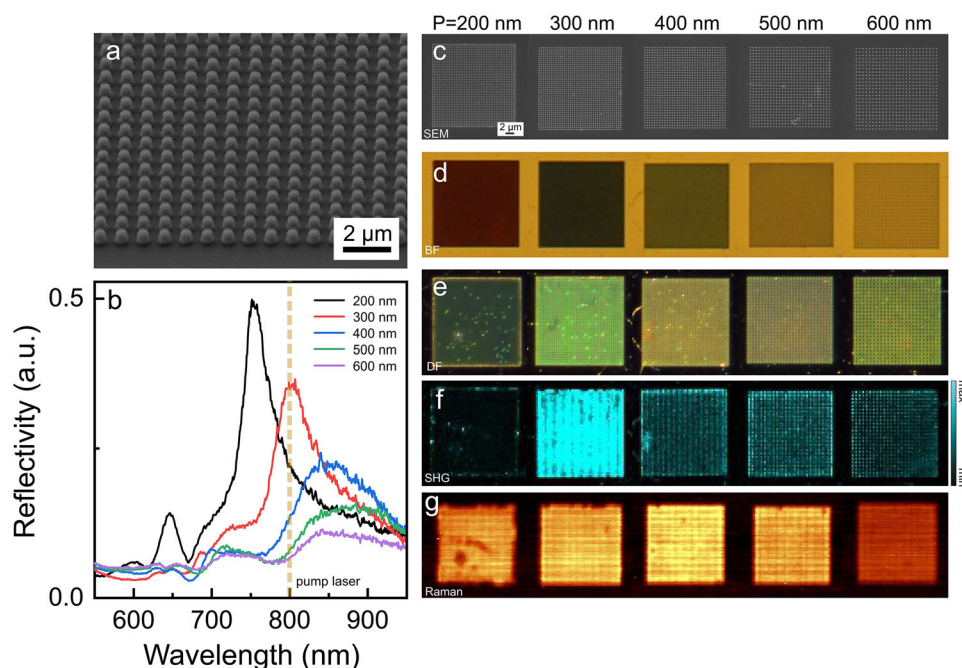


**Figure 2.** Arrays of WS<sub>2</sub>/TMD nanodisks. a) Tilted-view SEM image of TMD nanodisk array with diameter  $D = 250$  nm and pitch  $P = 200$  nm. b) Quasi-normal incidence ( $NA = 0.45$ ) reflection spectra from TMD nanodisk arrays with  $D = 250$  nm and  $P$  varying from 200 to 600 nm. c–e) Images of TMD nanodisk arrays with  $D = 250$  nm and  $P$  varying from 200 to 600 nm using: c) scanning electron microscopy, d) bright-field optical microscopy, and e) dark-field optical microscopy. f) Corresponding second-harmonic generation (SHG) maps probed at 400 nm. The false color-coded signal represents the intensity of the SHG signal. g) Wavenumber-specific confocal Raman maps probed at Raman peak of WS<sub>2</sub> at  $415\text{ cm}^{-1}$ . The Raman maps confirm complete removal of WS<sub>2</sub> in the etched region around disk arrays, and no damage of the etched disks.

as Mie resonances of individual disks, and lattice modes formed due to far-field couplings in periodic systems.<sup>[5,9,16,33,34]</sup>

## 2.1. Nanodisk Arrays

**Figure 2** summarizes our results on nanodisk arrays made of multilayer WS<sub>2</sub>. The samples were fabricated by a combination of electron beam lithography (EBL) and reactive ion etching (RIE), see Experimental Section. For simplicity, in this study we restrict ourselves to square nanodisk arrays. However, more complex array symmetries are equally possible with the use of EBL. As a proof-of-concept, first, we fabricated WS<sub>2</sub> nanodisk lattices with various pitches ( $P$ : in the 200–600 nm range with a step of 100 nm) and disk diameters ( $D$ : 200 and 250 nm) on a transparent SiO<sub>2</sub> substrate (Figure 2a). Here, we take advantage of our previous nanofabrication recipes<sup>[5,8]</sup> and develop them further.

Briefly, mechanically exfoliated WS<sub>2</sub> flakes ( $L = 90$  nm) were transferred onto a SiO<sub>2</sub> substrate using a dry-transfer method.<sup>[35]</sup> Nanofabrication of TMD nanostructures on silicon substrates with thin thermal oxides is relatively straightforward and was addressed in our previous studies.<sup>[5,8,9]</sup> On the other hand, it is demanding to fabricate TMD nanostructures on transparent, low refractive index, and non-conductive substrates, such as SiO<sub>2</sub>. Nanostructures on microscope cover glasses are useful for practical applications, as they allow to monitor the sample using high numerical aperture (NA) immersion objectives in both transmission and reflection modes. Specifically, use of a negative resist on top of a non-conductive glass substrate, a method which

yields high-quality TMD nanostructures, increases fabrication complexity. Therefore, one of the practical goals of this study is to develop a recipe for fabrication of high-quality TMD nanostructures not only on standard silicon substrates, but also on other substrates such as non-conductive, transparent thin glass substrates for future nanophotonic applications.

Our recipe to fabricate TMD nanodisk arrays on a glass substrate with a negative resist is the following. We start with deposition of a negative e-beam resist (MaN-2405) on the substrate by spin coating at 3000 rpm, which is followed by soft baking at 90 °C to prepare an etching mask. It is worth mentioning that other standard negative resists for example, HSQ can also be used to prepare the etching mask. The main issue for applying the resist homogeneously onto TMD flakes on a substrate is adhesion of the resist. Our solution to the problem is applying the TI:Prime adhesion promoter prior to the resist deposition. As an alternative, a standard HMDS adhesion promoter can be used. However, application of HMDS results in less reproducible results since this material is more sensitive to ambient conditions, in contrast to TI:Prime, which is why we chose to work with the latter.

To achieve high-quality densely packed TMD nanodisk arrays with EBL, the resist should be typically pre-coated with a reflective and conductive thin layer of chromium (Cr, 20 nm) in order to i) suppress electron beam scattering in the resist due to the proximity effect, and ii) for better focusing of the e-beam on the resist surface. However, removing the Cr layer after the exposure is an issue and is not compatible with the MaN-2405 negative resist, since the standard wet-etchant for Cr chemically modifies



the resist during etching, which in turn results in a problem for further development of MaN-2405. One solution to this problem could be replacing the Cr layer with a water-soluble conductive polymer (e-spacer) film. However, using an e-spacer polymer in combination with a thick negative resist on a non-conductive substrate results in poor mask quality for later fabrication stages. Therefore, our solution to the problem is to combine the water-soluble e-spacer with the reflective Cr layer to achieve the best quality sample. To that end, the water-soluble e-spacer is spin-coated directly on the resist at 2000 rpm for 20 s before depositing the Cr layer. This results in a higher quality of the etching mask after the development process, since removal of the Cr layer can be done simply by rinsing with running water for a few seconds. In this process, one needs to be careful and treat the sample gently since the TMD flake is at risk of delamination from the substrate because of weak vdW forces acting between them. After removing the Cr layer, the exposed sample is developed using the MaD-525 developer, followed by rinsing with water. The sample is then dry-etched in an inductively coupled plasma RIE using CHF<sub>3</sub> gas (see Experimental Section).

Since we use CHF<sub>3</sub> as a main etching gas, the top resist may get hardened because of carbon redeposition in the presence of fluorine ions. This leads to two consequences: i) a positive one: it allows us to perform longer etching due to the hardened resist mask and ii) a negative one: it may lead to an unwanted issue of removing the left-over resist after the etching. To resolve the negative consequence of carbon re-deposition, we perform additional oxygen plasma stripping with O<sub>2</sub> (40 sccm) after the dry etching. This removes the top hardened resist layer. Subsequently, the left-over resist can be easily removed by exposure to hot acetone (50 °C) for 3 min, followed by rinsing with isopropyl alcohol and deionized water.

After fabrication we characterized the WS<sub>2</sub> nanodisk samples using several spectroscopy and microscopy techniques. First, we measured reflection spectra under quasi-normal incidence using a long working distance 20× objective (Nikon, NA = 0.45) (see Experimental Section). Figure 2b shows normal-incidence reflection spectra from WS<sub>2</sub> nanodisk lattices with diameter  $D = 250$  nm and pitch ( $P$ ) varying from 200 to 600 nm. Their corresponding scanning electron microscopy (SEM), bright-field (BF), and dark-field (DF) images are shown in Figure 2c–e, respectively. Our results demonstrate the appearance of lattice modes in WS<sub>2</sub> nanodisk arrays that can be tuned by controlling the geometrical parameters of the sample, such as  $D$  and  $P$ . These structures exhibit bright colors across the entire visible range. The colors depend on the structure of the nanoparticle array, including individual nanodisk height and radius, as well as the array arrangement (see Figure 2d,e). The peaks in the reflection spectra plotted in Figure 2b originate from nanodisk ( $D = 250$  nm) arrays with various  $P$ . The measured spectra agree reasonably well with the simulated ones, presented in Figure S2, Supporting Information, for nanodisk arrays with geometric parameters corresponding to the fabricated samples. In particular, the simulated spectra predict prominent reflection peaks for  $P = 200$  and 300 nm samples. These peaks are Rayleigh diffractive anomalies occurring at the onset of  $(\pm 1, 0)$  and  $(0, \pm 1)$  diffraction orders in glass substrate upon normal-incidence illumination. This is verified by calculating the Rayleigh wavelengths as  $\lambda_R = n_{\text{sub}}(P + D)$  and comparing those to the spectral position of the corresponding peaks in

the measured spectra. Measured and simulated data obtained for nanodisk arrays with  $D = 200$  nm are summarized in Figures S1 and S2, Supporting Information.

Furthermore, we performed additional measurements to demonstrate the angular dispersion behavior of the lattice modes (see Figure S4, Supporting Information). Our results show that the peaks in the reflection spectra exhibit clear lattice-like angular dispersion behavior. Due to the fact that the peaks in reflection show a clear  $P$ -dependence with fixed  $D$  as well as angular dispersion, they can be interpreted as lattice modes induced by the periodic arrangement of WS<sub>2</sub> nanodisks.

Next, we studied second-harmonic generation (SHG) from the fabricated WS<sub>2</sub> nanodisk arrays. SHG measurements were carried out using a home-built optical setup, coupled to a tunable (690–1040 nm) Ti:sapphire femtosecond laser. Excitation wavelengths were varied between  $\lambda_{\text{exc}} = 770, 800, 850, 900,$  and 950 nm to match the resonances of the lattice modes in the WS<sub>2</sub> nanodisk arrays with different  $P$ .

First, we carried out the power-dependent SHG measurements from an array and obtained the slope-2 in logarithmic scale to prove that the collected signal originates from SHG (Figure S5, Supporting Information). It is known that unpatterned multilayer WS<sub>2</sub> flakes exhibit a negligible SHG signal due to the centrosymmetric nature of the AB-stacked bulk crystal. Therefore, it is interesting to verify whether nanopatterning can enhance and modify SHG in a multilayer WS<sub>2</sub> sample. Several examples for SHG imaging ( $\lambda_{\text{SHG}} = 400$  nm) from WS<sub>2</sub> nanodisk ( $D = 250$  nm) arrays with various  $P$  under  $\lambda_{\text{exc}} = 800$  nm excitation are shown in Figure 2f (note false color). Interestingly, we observed that when the lattices are resonantly pumped with  $\lambda_{\text{exc}}$  that spectrally overlaps with the lattice modes, SHG imaging shows the highest intensity from the resonant array. One can clearly see that the nanodisk ( $D = 250$  nm) array with  $P = 300$  nm shows the highest SHG intensity due to the resonant excitation of  $\lambda_{\text{exc}} = 800$  nm, whereas  $P = 200$  nm gives much lower SHG intensity because of the poor spectral overlap with the lattice mode. On the other hand, when we pumped all nanodisk arrays by  $\lambda_{\text{exc}} = 770$  nm, the  $D = 250$  nm array with  $P = 200$  nm resulted in the highest SHG intensity due to the better resonant excitation (see Figures S6 and S8, Supporting Information). The data from  $D = 200$  nm samples are summarized in Figure S7, Supporting Information. Our observations suggest that the SHG signal from the WS<sub>2</sub> nanodisk arrays can be enhanced by controlling the optical resonances through nanopatterning. Such enhancement occurs despite the absence of broken inversion symmetry in the bulk WS<sub>2</sub> crystal. Thus, the origin of SHG in this case is likely the surface and edges exposed through nanopatterning.

This suggests that in order to attain the highest SHG intensity enhancement one should maximize the surface area of the nanostructure and at the same time maintain high electric field intensity at the surface, which calls for a non-trivial optimization procedure. Resonant modes of individual nanoantennas, as well as the diffractive interactions within the array, have been previously shown to enhance the SHG intensity in TMD metasurfaces.<sup>[6,24,25]</sup> The results observed with our arrays can probably be explained by similar mechanisms; given the dimensions of the individual nanodisk and the excitation wavelength, the dipole and quadrupole Mie resonances are expected to play the key role in the SHG enhancement.

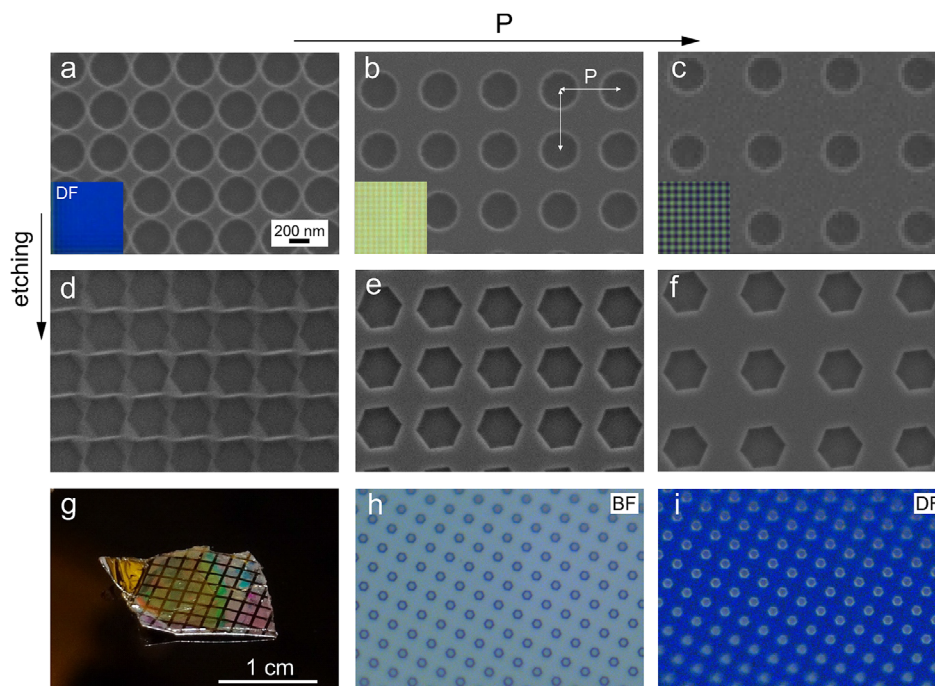


**Figure 3.** Arrays of TMD nanoholes. a–c) SEM images of nanohole arrays with  $D = 400$  nm and  $P = 100, 300$ , and  $500$  nm before anisotropic wet-etching. Insets show true-color dark-field optical microscope images of the corresponding arrays. d–f) SEM images of the same nanohole arrays as in (a–c) after anisotropic wet-etching. g) Optical image of a large-scale (over 1 cm in lateral dimensions) nanopatterned multilayer  $\text{WS}_2$  crystal. Each colorful pattern in the image is induced by periodically arranged lattices of microholes ( $D = 1$   $\mu\text{m}$ ) with  $P = 2$   $\mu\text{m}$ . h) BF and i) DF images of a hexagonal hole array taken from the large-scale nanopatterned flake.

To verify that the  $\text{WS}_2$  flake was etched completely into nanodisk arrays, we performed confocal Raman mapping. The Raman spectra show two clear Raman peaks at 349 and 415  $\text{cm}^{-1}$ , revealing that nanopatterned  $\text{WS}_2$  was not damaged (see Figure S9, Supporting Information). Figure 2g shows confocal Raman maps at 415  $\text{cm}^{-1}$  obtained from the  $\text{WS}_2$  nanodisk arrays. Raman maps confirm the complete removal of  $\text{WS}_2$  in all regions except for the lattice. In Figure 2g, the relative intensity of the Raman signal shows neither noticeable enhancement nor clear correlations with array pitches and features in the reflectivity spectra. When the pitch of the array increases, it shows slight reduction in Raman intensity due to less  $\text{WS}_2$  material per area. Raman spectroscopy of  $\text{MoS}_2$  nanocones was previously reported to be a useful tool for optically assessing the anisotropy of the system.<sup>[8]</sup> In this study, Raman spectroscopy was mainly used to monitor the completeness of etching. It is also worth mentioning that Raman mapping was carried out after all other optical characterizations, to prevent potential photodamage by strong laser irradiation. This precaution was motivated by our previous observations of unpatterned  $\text{WS}_2$  flakes being damaged during Raman mapping, probably because of the spectral overlap of the excitation laser ( $\lambda_{\text{exc}} = 532$  nm) with the absorption band of  $\text{WS}_2$  that can lead to unwanted heating.

## 2.2. Nanohole Arrays

The next class of structures we investigated was the nanohole arrays in TMD multilayers. The possibility to fabricate high qual-

ity TMD nanohole arrays of various sizes could open several applications ranging from metamaterials<sup>[36]</sup> to catalysis<sup>[29,37]</sup> and sensing.<sup>[38]</sup> Here, we address fabrication of nanohole arrays not only in few-hundred-micron TMD flakes, but also in macroscopic cm-scale TMD crystals. **Figure 3** shows a summary of the obtained  $\text{WS}_2$  nanohole arrays. Similar to the arrays of nanodisks, the samples were fabricated by a combination of EBL and RIE. The difference was, however, that this procedure was subsequently followed by anisotropic wet-etching to obtain hexagonal nanohole arrays terminated by zigzag edges<sup>[9]</sup> (Experimental Section). In contrast to the nanodisk arrays, here, we employed a positive resist (ARP 6200.13). First, we fabricated nanohole arrays in mechanically exfoliated  $\text{WS}_2$  flakes on a transparent and non-conductive glass substrate. The resist (ARP 6200.13) was spin-coated at 3000 rpm, followed by soft baking at 120 °C for 5 min. Subsequently, a thin layer of Cr (20 nm) was deposited directly on top of the resist without any additional e-spacer layer. This simplifies nanopatterning since ARP6200.13 is not modified during Cr removal by the standard Cr etchant (unlike the negative MaN-2405 resist used for nanodisk arrays). TMD flakes are immobilized and protected under the unexposed resist during the development process in *n*-amyl acetate. After development, the sample was etched using a dry RIE process, followed by a few seconds of additional oxygen plasma treatment and removal of the leftover resist in hot acetone. Figure 3a–c shows the fabricated  $\text{WS}_2$  circular nanohole arrays along with their corresponding DF images. An important difference of nanohole arrays (in comparison to nanodisks) is that they can be selectively wet-etched to produce nearly atomically sharp edges with

exclusive zigzag terminations (Figure 3d–f).<sup>[9]</sup> This method was employed to obtain TMDs with sharp zigzag edges after lithography and dry etching processes. Specifically, the sample was exposed to an aqueous solution containing  $\text{H}_2\text{O}_2$  and  $\text{NH}_4\text{OH}$  (1:1:10  $\text{H}_2\text{O}_2$ : $\text{NH}_4\text{OH}$ : $\text{H}_2\text{O}$  volume ratio of stock solutions under mild heating at  $T = 50^\circ\text{C}$ ). This led to formation of well-defined hexagonal holes from pre-patterned circular holes due to anisotropic wet-etching. The resulting zigzag edges could carry a set of useful multi-functional properties, including catalytic activity for hydrogen evolution<sup>[37,39]</sup> and enhanced charge transport.<sup>[40]</sup> Recently, a similar nanofabrication approach using hBN as an etching mask and resulting in nanoholes down to  $\approx 20$  nm has been introduced.<sup>[41]</sup>

During anisotropic wet-etching the armchair edges are etched much faster than the zigzag edges, probably because of differences in their chemical reactivity. The resulting nanohole arrays are terminated by sharp zigzag edges, which make them potentially interesting for applications. For instance, zigzag edges have been predicted to be metallic and ferromagnetic, in contrast to ordinary semiconducting armchair edges.<sup>[42–44]</sup> Zigzag edges could also be useful for high electro- and photo-catalytic activity.<sup>[45]</sup> Moreover, they show potential for nonlinear optics applications, such as enhanced second-harmonic generation.<sup>[46]</sup> In a previous study, we showed that standard  $\text{WS}_2$  can be tailored with multi-functional atomically sharp zigzag edges using a facile wet-etching technique that uses only abundant and environmentally friendly chemicals.<sup>[9]</sup> Here, we expand this technique to other parameter ranges, improve the nanofabrication procedure, and apply it to macroscopic samples, as we show below.

In addition to the microscopic samples, we fabricated a large-area nanostructured TMD sample in a macroscopic  $\text{WS}_2$  crystal (size of  $\approx 1$  cm in lateral dimensions, see Figure 3g–i). The sample was fabricated in a similar manner to the microscopic hole array samples—by a combination of EBL and RIE, followed by anisotropic wet-etching. To do so, we transferred a few  $\mu\text{m}$  thick  $\text{WS}_2$  crystal onto a silicon substrate (Figure 3g). It is worth mentioning that, in principle, any substrate can be employed or even a bulk TMD crystal can be directly nanopatterned without any additional substrate. Figure 3g shows an optical image of a nanopatterned  $\text{WS}_2$  crystal. Colorful square-patterns on the crystal surface are due to periodically arranged micron-sized holes with a pitch of  $2\ \mu\text{m}$  (see Figure 3g). The depth of the etched holes is  $\approx 3\ \mu\text{m}$ . BF and DF images of these hole arrays are shown in Figure 3h,i, respectively.

The advantage of a large-scale nanostructured TMD can be twofold. First, it allows preparing nanostructured TMD samples without any resist contamination, by exfoliation directly from the pre-patterned  $\text{WS}_2$  crystal. We have exfoliated high quality nanostructured TMD samples onto polydimethylsiloxane (PDMS) stamps by employing the standard scotch-tape method from the macroscopic patterned crystal shown in Figure 3g. Later, these samples can be transferred onto any desired substrate for further use. Second, large scale nanopatterned TMDs may be of interest in their own right, since a combination of high surface-to-volume ratio and multi-functional zigzag edges over a large area make them useful for applications in photo- and electro-catalysis<sup>[37,45]</sup> and sensing.<sup>[38]</sup> Moreover, the colorful patterns in nanostructured TMD crystals could be useful for structural color and opto-electronic applications. Additionally, this large-

scale sample provides evidence that the fabrication techniques developed in this work are potentially scalable and currently limited only by the lateral size of the original TMD crystal.

### 3. Nanostructured TMDs for Light Confinement and Waveguiding

The nanostructures and their applications discussed above are based on a combination of high refractive index, optical anisotropy, and high absorption.<sup>[11,47–49]</sup> However, TMDs can also support an alternative scenario—the one in which the optical losses are low, while high refractive index and optical anisotropy are preserved.<sup>[5,11,12,14]</sup> This is realized in the near-infrared spectral range in the case of semiconducting TMDs and can offer novel applications of TMD nanostructures for low-loss nanophotonics, such as high quality factor ( $Q$ ) resonators and waveguides. The combination of low-loss, high refractive index, optical anisotropy, and mechanical flexibility<sup>[10]</sup> can potentially enrich low-loss nanophotonic applications.<sup>[18]</sup>

To make initial steps toward testing these predictions, we have fabricated several proof-of-concept devices (Figure 4). Here, we choose multilayer  $\text{WS}_2$  to fabricate various low-loss nanophotonic devices that can potentially operate at the telecom range (1550 nm). This choice is motivated by the lowest optical loss in  $\text{WS}_2$  in comparison to other typical TMDs, because the excitonic features (A, B, C excitons) in  $\text{WS}_2$  appear at lower wavelengths than in other TMDs. Figure 4a shows a ring resonator coupled to two waveguides. The sample was fabricated starting from a  $L = 150$  nm thick multilayer  $\text{WS}_2$  on a thermally oxidized silicon substrate with a  $3\ \mu\text{m}$   $\text{SiO}_2$  layer by employing a negative resist (MaN-2405). First, the flake was transferred onto a substrate using a dry transfer technique. The thickness of the flake was measured by a profilometer. Subsequently, MaN-2405 (500 nm) negative resist was spin-coated for the EBL step. To prevent the adhesion issue of the resist, either the TI:Prime adhesion promoter or a thin layer of  $\text{SiO}_2$  can be deposited. After the standard EBL process, the resist was developed in the MaD-525 developer to prepare the etching mask. Various designs of microrings and waveguides were fabricated from the multilayer  $\text{WS}_2$  flake by dry RIE technique (see Figure 4a–c for top and tilted-view SEM images). BF and DF images of an exemplary device are shown in Figure 4d,e, respectively.

After fabrication we proceeded with testing light coupling into the devices. Specifically, we coupled a broadband white light source (laser-driven white light source, LDLS) into an input channel of the waveguide using a high numerical aperture objective (40 $\times$ , NA = 0.95). As shown in Figure 4e, light was transmitted through the waveguide, and the other (output) end of the waveguide was lit up showing a proof-of-concept possibility for TMD-based low-loss photonic devices.

Although we have not carried out optical characterizations of the fabricated devices, we simulated their performance using the finite-difference time-domain (FDTD) method. The simulated data suggest excellent properties of  $\text{WS}_2$  waveguides and ring resonators (see Figure S10, Supporting Information). While the simulated device was not optimized, it shows decent transmission properties with only small reflections at the couplers and very small scattering due to the square meshing of the ring. Our findings are in line with recent calculations suggesting that TMDs



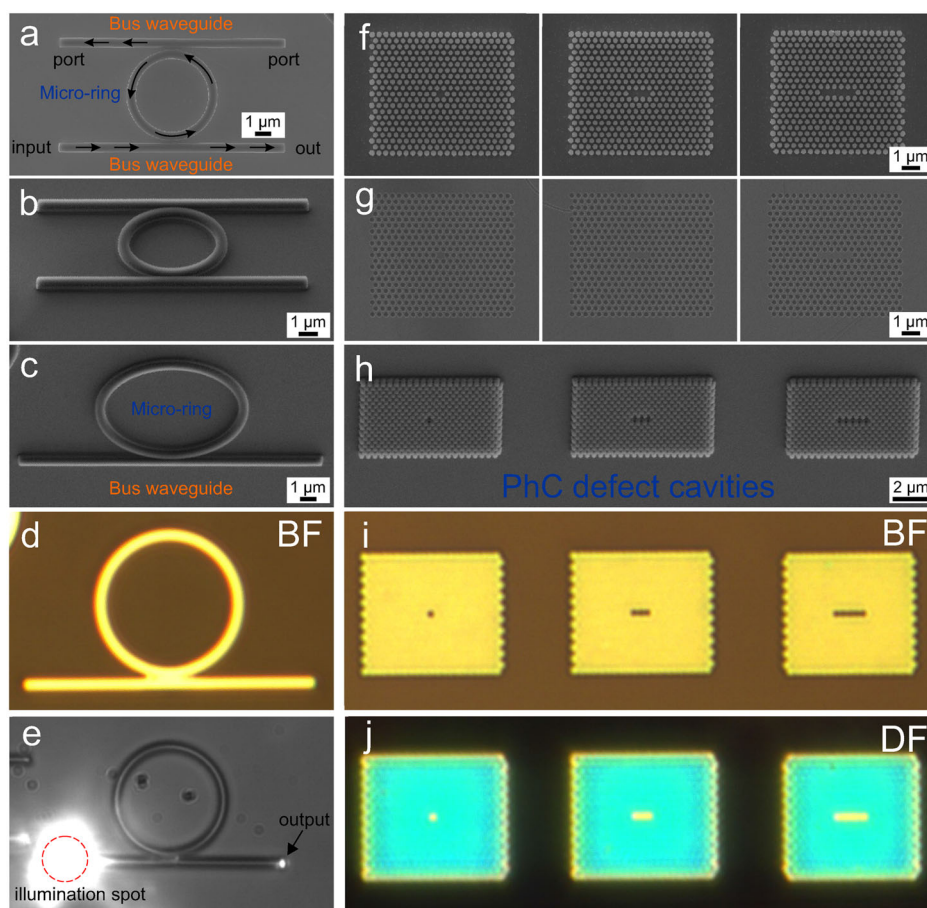


**Figure 4.** Exemplary low-loss TMD nanophotonics devices. a–e) SEM, BF, and DF images of the fabricated  $\text{WS}_2$ -based nanophotonic circuits consisting of waveguide-coupled  $\text{WS}_2$  microring resonators. a–c) SEM images of exemplary ring resonators coupled with bus waveguides that are made of  $\text{WS}_2$ : top-view (a), tilted-view of a ring resonator coupled to two bus waveguides (b), and tilted-view of a ring resonator coupled to single bus waveguide (c), respectively. In (d), optical BF image of exemplary device is displayed. e) Demonstrates a proof-of-concept possibility of TMD-based waveguide by showing that injected light to the input port was transmitted through the waveguide and the other (output) end of the waveguide was lit up. f–j) The same as (a–e) for a series of exemplary photonic crystal cavities fabricated from a 300 nm thick  $\text{WS}_2$  film on top of glass. (f–h) show SEM images of the fabricated photonic crystals consist of either  $\text{WS}_2$  nanodisk array or nanohole arrays. Corresponding BF and DF optical images are displayed in (i) and (j), respectively.

could be an excellent low-loss nanophotonics platform.<sup>[18]</sup> In our work, we report the first nanofabrication attempts toward realization of this vision.

In addition to the waveguides and ring resonators, we also explored the fabrication of TMD photonic crystal cavities. Perturbing a number of unit cells in a periodic 2D array (for example, removing a series of holes or disks from an array of those) results in the emergence of photonic crystal defect cavities supporting finite lifetime resonances.<sup>[50]</sup> Starting from a 300 nm thick  $\text{WS}_2$  flake on top of a glass substrate hosting a triangular array of holes with a radius of 120 nm and a lattice constant of 400 nm, we fabricated L1, L3, and L5 defect cavities by removing 1, 3, or 5 holes in a row from the periodic array, respectively.

Figure 4f–j shows top and tilted-view SEM images as well as BF and DF images of the fabricated photonic crystal cavities. Since optical characterization of photonic crystal cavities is challenging with far-field spectroscopy and traditionally relies on near-field spectroscopy (or on-chip circuitry), we turned to numerical simulations of the fabricated photonic crystal cavities. Figure S11,

Supporting Information, presents the resulting electric field distributions of the L1, L3, and L5 cavity modes revealing their fundamental resonances at 1556, 1690, and 1705 nm, respectively. The experimental confirmation of these theoretical predictions is a subject of future work.

### 3.1. Nanopatterning of In-Plane Anisotropic and Metallic Materials

So far we have discussed nanostructuring of standard semiconducting in-plane isotropic TMD materials, such as  $\text{WS}_2$ . However, many TMD materials can be found in other forms, including hyperbolic, and in-plane anisotropic phases. Optical properties of such TMDs are of certain interest and their nanostructuring can open additional means to manipulate light on the nanoscale. Motivated by this, here we developed ways to nanopattern several more exotic TMD materials, including  $\text{ReS}_2$ ,  $\text{TaSe}_2$ ,  $\text{TaS}_2$ , and  $\text{NbSe}_2$ . These materials possess remarkable



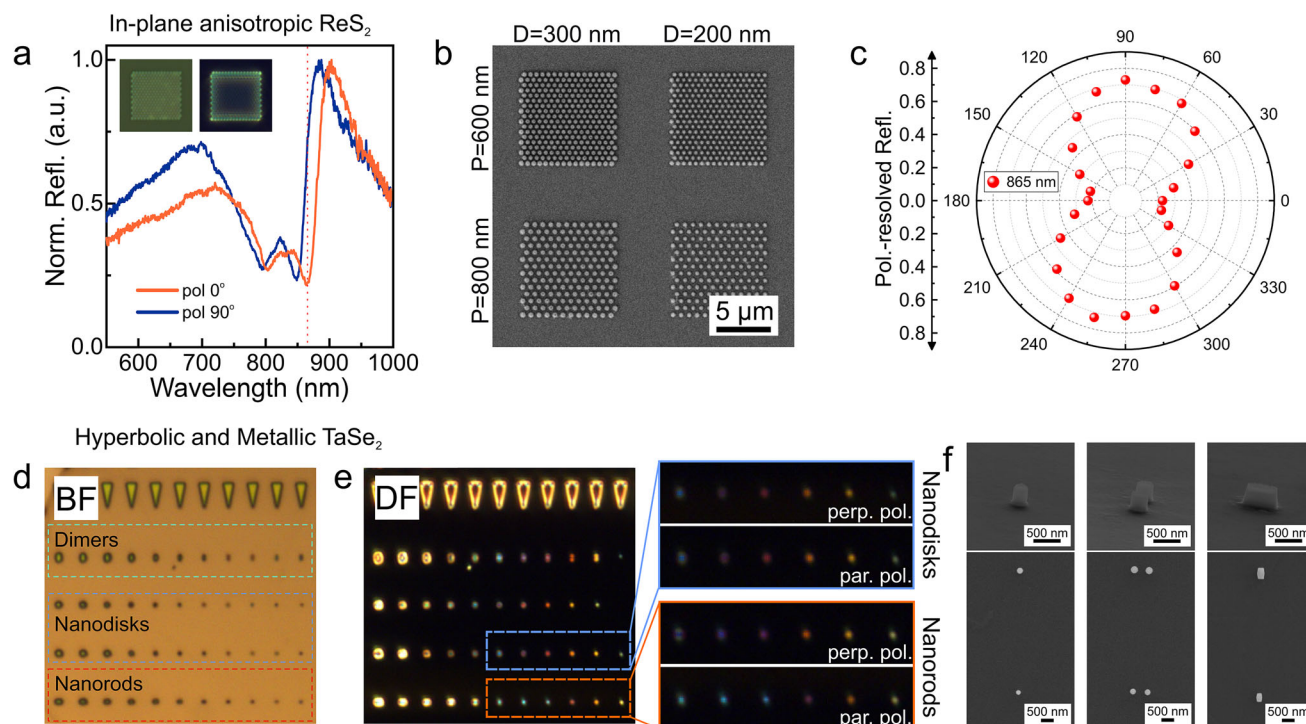


**Figure 5.** In-plane anisotropic  $\text{ReS}_2$ . a) Reflection spectra at pol-0 (orange) and pol-90 (blue), b) SEM image, and c) polarization-resolved reflection shown as a polar plot at 865 nm measured from an exemplary  $\text{ReS}_2$  nanodisk hexagonal arrays with  $D = 300$  and  $200$  nm (left and right columns), and  $P = 600$  and  $800$  nm (top and bottom rows), respectively. Inset in (a) shows DF and BF images of the nanodisk hexagonal array ( $D = 300$  nm,  $P = 800$  nm). Hyperbolic and metallic  $\text{TaSe}_2$ . d) BF and e) DF images of  $\text{TaSe}_2$  single nanodisks, nanodisk dimers, and nanorods with various sizes, respectively. Diameter of individual  $\text{TaSe}_2$  nanodisks were varied ranging from  $100$  to  $1100$  nm, whereas nanorods were elongated with the aspect ratio (AR) of  $2$  along one of the axes. Height is  $150$  nm. Inset shows DF images of nanodisks ( $D: 100\text{--}600$  nm) and nanorods ( $W: 100\text{--}600$  nm, with AR:2) taken under perpendicular and parallel polarization with respect to the longer axis of the nanorod. f) Corresponding tilted- and top-view SEM images of exemplary  $\text{TaSe}_2$  single nanodisk, dimer, and nanorod, respectively.

properties, for instance,  $\text{ReS}_2$  is in-plane anisotropic due to its stable  $1T'$ -distorted phase, while  $\text{TaSe}_2$ ,  $\text{TaS}_2$ , and  $\text{NbSe}_2$  are in-plane isotropic, metallic and even superconducting at low temperatures. Nanopatterning of these more exotic TMD materials can further enrich their properties and open new directions in nanophotonics and nanoelectronics.

We performed several important tests in order to develop a viable nanofabrication strategy for exotic TMDs for example,  $\text{ReS}_2$ ,  $\text{TaSe}_2$ ,  $\text{TaS}_2$ , and  $\text{NbSe}_2$  (see Figure 5 and Figure S12, Supporting Information). We started with  $\text{ReS}_2$  that is characterized by different in-plane permittivity tensor elements ( $\epsilon_{xx} \neq \epsilon_{yy}$ ) and thus enables an in-plane anisotropic optical response. By designing geometrically symmetric nanophotonic structures out of  $\text{ReS}_2$  with its intrinsic in-plane anisotropy, one could envision photonic crystal structures where polarization-degeneracy would be lifted up. This can be an interesting approach to fabricate, for example, elliptical photonic cavities.<sup>[51]</sup> To demonstrate this possibility in a nanofabrication experiment, we successfully etched nanodisk hexagonal arrays with various dimensions out of  $120$  nm thick multilayer  $\text{ReS}_2$  flake using a combination of EBL and dry etching with  $\text{CHF}_3$  (Figure 5a–c). It is important to note that the etching rate of  $\text{ReS}_2$  with a standard  $\text{CHF}_3$  gas was about  $3\times$  slower ( $\approx 3$  nm  $\text{min}^{-1}$ ) than more conventional TMDs ( $10$  nm  $\text{min}^{-1}$ ). This suggests that the etching process for  $\text{ReS}_2$  is more physical than chemical. The problem is that the selectivity of physical etch-

ing is, in general, poor and it also requires relatively thick resists. Therefore, the nanostructuring of thick  $\text{ReS}_2$  requires further optimization steps and improvements. As a potential improvement, we propose that etching with other chemicals, such as  $\text{SF}_6$  or  $\text{Cl}$ -based gases, could make the process more chemical. Another suggestion is to perform etching using hard etching masks such as chromium or aluminum.

Figure 5a shows reflection spectra of an exemplary  $\text{ReS}_2$  nanodisks hexagonal array ( $D = 300$  nm,  $P = 800$  nm) with two orthogonal polarizations. As is seen, the polarization dependence of the  $\text{ReS}_2$  array is anisotropic, due to the in-plane anisotropic crystalline structure of the bulk material. This allows to selectively excite the resonances of the array by tuning the polarization of the light at certain wavelengths. An exemplary SEM image of the  $\text{ReS}_2$  array is shown in Figure 5b, which confirms our nanofabrication strategy is successful and applicable to  $\text{ReS}_2$ . Furthermore, the polar plot in Figure 5c shows polarization-resolved reflection at  $865$  nm (close to maximum anisotropy), demonstrating pronounced optical anisotropy inherited from the bulk crystal. Such anisotropy implies that nanostructured multilayer  $\text{ReS}_2$  could be useful for SHG applications due to its natural broken inversion symmetry. Moreover,  $\text{ReS}_2$  nanostructures could gain an additional tunability feature thanks to a recently demonstrated optically-induced switching in nonlinear optical response.<sup>[52]</sup>

Furthermore, we fabricated TaSe<sub>2</sub> nanodisks and nanorods out of 150 nm freshly exfoliated TaSe<sub>2</sub> flake. This material has a metallic response for in-plane electronic excitations (with the plasma frequency in the near infrared range), while a dielectric response for out-of-plane electronic excitations, which means the material is naturally hyperbolic. BF, DF, and SEM images of the prepared samples are shown in Figure 5d,e. TaSe<sub>2</sub> nanodisks were fabricated with various diameters ranging from 100 to 1100 nm, whereas nanorods were elongated with the aspect ratio (AR) of 2 along one of the axes. In Figure 5e, one can clearly observe size- and shape-dependent colors in the DF image, in line with a typical plasmonic and dielectric nanophotonics size dispersion. Polarization-resolved DF images in the inset of Figure 5e were obtained under perpendicular and parallel polarizations with respect to the long axis of the nanorod. Polarization-resolved DF images from TaSe<sub>2</sub> nanodisks (*D*: 100–600 nm) exhibit identical symmetric response under different polarizations. On the other hand, elongated TaSe<sub>2</sub> nanorods (AR = 2) show polarization-dependent response due to asymmetric geometry. Measured DF scattering spectra taken from individual TaSe<sub>2</sub> nanodisks and nanorods are summarized in Figure S13, Supporting Information. Since the plasma frequency of TaSe<sub>2</sub> and similar metallic TMDs occurs in the near-infrared region around ≈1000–1300 nm,<sup>[53]</sup> a successful nanostructuring of such hyperbolic TMDs could lead to a combined 2-in-1 plasmonic-high-index-dielectric response in the visible–near-infrared range, with plasmonic response dominating at frequencies below the plasma frequency, while dielectric response—at frequencies above it. Our nanofabrication strategy successfully demonstrates the feasibility of this approach.

## 4. Conclusion

In conclusion, in this work we propose a roadmap of all-TMD nanophotonics for light absorption and light confinement and guiding. We demonstrate several viable nanofabrication strategies toward reaching key nanophotonic building blocks, including nanodisk and nanohole arrays, ring resonators, waveguides, and photonic crystals on several relevant substrates. TMD nanophotonics may take advantage of TMD's remarkable intrinsic optical properties, namely, high refractive index ( $n \approx 4$ ), low optical loss (in the near-infrared region), in-plane and out-of-plane anisotropy ( $\epsilon_{xx} = \epsilon_{yy} \neq \epsilon_{zz}$  and  $\epsilon_{xx} \neq \epsilon_{yy} \neq \epsilon_{zz} \neq \epsilon_{xx}$ , respectively), and hyperbolicity ( $\epsilon_{xx} = \epsilon_{yy} < 0$  and  $\epsilon_{zz} > 0$ ). Special attention was devoted to nanofabrication on non-conductive transparent substrates (SiO<sub>2</sub>), which are commonly used in nanophotonic applications. The nanofabrication methods developed in this work are desperately needed to open new possibilities for TMD nanophotonics.<sup>[18]</sup> We envision that nanostructured TMDs will enrich the toolbox of available materials for light absorption, waveguiding, metasurfaces, and other applications.

## 5. Experimental Section

**Sample Fabrication:** TMD flakes were mechanically exfoliated from bulk crystals (HQ-graphene) onto PDMS stamps using the scotch-tape method, and then transferred onto various substrates (mostly glass substrates in this study) using the all-dry-transfer method.<sup>[35]</sup> Thicknesses

of the transferred TMD flakes were measured using a VEECO profilometer. Nanopatterning of the TMD flakes was achieved by a combination of electron-beam exposure of negative or positive resists with a dry etching.

**Nanopatterning the Multilayer TMDs with a Positive Resist:** First, the etching mask for nanopatterning the TMD flakes was carried out by spin coating a positive resist of ARP 6200.13 at 3000 rpm for 1 min, which yielded a ≈500 nm thick resist. Then, the samples were baked on a hotplate at 120 °C for 5 min, followed by deposition of a thin chromium (Cr, 20 nm) layer for EBL on a non-conductive glass substrate. Subsequently, samples were exposed using a JEOL JBX 9300FS EBL system, operated at 100 kV. The alignment of the flakes was ensured using pre-fabricated gold markers on the substrate. After the e-beam exposure, the Cr layer was removed using a Cr remover, followed by rinsing the sample with deionized (DI) water. Then, the samples were developed in an *n*-amyl acetate solution for ≈5 min, and dried with nitrogen gas, to prepare the etching mask. The etching of the samples was performed in an inductively coupled reactive ion etcher (RIE) with CHF<sub>3</sub> (50 ccm) and Ar (40 ccm) at a pressure of 10 mTorr and accelerated by 50 W forward power. After the dry etching, oxygen plasma stripping with O<sub>2</sub> (40 sccm) was carried out to remove the top hardened resist layer. As a last step, the left-over resist mask was removed by acetone at 50 °C for 3 min, followed by rinsing the sample with isopropyl alcohol and DI water. For further anisotropic wet-etching, the previously developed wet-etching method using an aqueous solution composed of H<sub>2</sub>O<sub>2</sub>:NH<sub>4</sub>OH:H<sub>2</sub>O was used.<sup>[9]</sup>

**Nanopatterning with a Negative Resist:** In order to fabricate nanodisks, ring resonators, and waveguides out of multilayer TMDs, a negative resist of MaN-2405 was employed for the etching mask.<sup>[5]</sup> A negative MaN-2405 resist was spin coated at 3000 rpm for 1 min, followed by soft baking on a hotplate at 90 °C for 1 min. For high-quality EBL on a non-conductive substrate, a conductive e-spacer ink was deposited by spin coating at 2000 rpm for 30 s, followed by deposition of a thin chromium (Cr, 20 nm) layer using a thermal evaporator. Subsequently, samples were exposed by an e-beam to design the etching mask. Then, both the conductive e-spacer and Cr layers were removed using running DI water. After removal of the conductive layer, the samples were developed using a MaD-525 developer for 60 s, followed by abundant rinsing with DI water. After the successful preparation of the etching mask, dry etching of the sample was performed in an inductively coupled RIE by CHF<sub>3</sub> (50 ccm) and Ar (40 ccm) at a pressure of 10 mTorr and accelerated by a 50 W forward power. To remove any left-over resist after etching, mild oxygen plasma stripping with O<sub>2</sub> (40 sccm) was carried out and followed by immersion in hot acetone at 50 °C for 3 min. Then, the samples were rinsed by isopropyl alcohol and DI water.

After nanopatterning, full optical characterization of the samples, including reflection, Raman and second-harmonic spectroscopy were performed. The scanning electron microscope imaging was performed using a Zeiss ULTRA 55 FEG.

**Reflection Spectroscopy and Dark-Field Imaging:** Bright-field reflection spectra at normal incidence were collected using a 20× air objective (Nikon, NA = 0.45), directed to a fiber-coupled spectrometer and normalized by reflection from a standard dielectric-coated silver mirror. Dispersion relations in reflection were obtained by a single-shot imaging using a 60× oil-immersion objective (Nikon, NA = 1.49) in the back-focal imaging setup. Back-focal plane images were scanned using an EM-CCD camera (Andor, iXon) combined with the tunable liquid crystal filter and analyzed to extract dispersion relations in reflection. The dark-field scattering images were obtained using an upright microscope (Nikon Eclipse LV150N) equipped with an air reflective dark-field objective lens (100×, NA = 0.8).

**Raman Spectroscopy:** Raman spectra were collected in a back-scattering geometry using a commercial Raman microscope (WITec alpha300R, 100× air objective), equipped with a scanning stage and using a  $\lambda_{\text{exc}} = 532$  nm CW-laser excitation.

**Second-Harmonic Generation:** SHG measurements were performed using a home-built microscope, which was coupled to a tunable (690–1040 nm) Ti:sapphire femtosecond laser (MaiTai HP-Newport Spectra-Physics) with 100 fs pulse duration and 80 MHz repetition rate. The excitation wavelengths were tuned to overlap with the peak resonances in the reflection spectra of the nanodisk arrays. The fundamental laser beam

was directed at the sample by passing through a dichroic mirror (Semrock, FF775-Di01-25×36). Then, the beam was focused on the sample, mounted at the piezo stage (Mad City Labs, Nano-LP200) using a 40× microscope objective (Nikon, NA = 0.95) with a spherical aberration correction ring to reduce the deterioration of the image due to the cover glass thickness. The SHG signal was collected in reflection by following the same optical path and separated from the fundamental beam using a dichroic mirror and a short pass filter (Semrock-FF01-720/SP-25). The collected beam was then focused on the entrance of a 50 μm multimode fiber, which was coupled to either a spectrometer (Andor 500i, equipped with Newton 920 CCD camera) or an avalanche photodiode (APD, IDQ, ID100 Visible Single-Photon Detector) in order to perform the SHG spatial mapping. For the SHG spatial mapping, the scanning piezo stage was used with a 0.4 nm accuracy and the SHG counts were detected by the APD.

## Supporting Information

Supporting Information is available from the Wiley Online Library or from the author.

## Acknowledgements

B.M., D.G.B, B.K., and T.O.S. acknowledge financial support from the Swedish Research Council (VR Miljö project, grant No: 2016-06059), the Knut and Alice Wallenberg Foundation (grant No: 2019.0140), Chalmers Excellence Initiative Nano and 2D-TECH VINNOVA competence center (Ref. 2019-00068). D.G.B. acknowledges Council on grants of the President of the Russian Federation (MK-1211.2021.1.2), BASIS Foundation (grant 22-1-3-2-1), and Russian Science Foundation (21-12-00316). T.J.A. thanks the Polish National Science Center for support via the project 2019/34/E/ST3/00359. This work was performed in part at the Myfab Chalmers cleanroom, and the Chalmers Material Analysis Laboratory, CMAL.

## Conflict of Interest

The authors declare no conflict of interest.

## Data Availability Statement

The data that support the findings of this study are available from the corresponding author upon reasonable request.

## Keywords

2D materials, nanophotonics, nanostructures, transition metal dichalcogenides

Received: January 26, 2022  
Revised: September 9, 2022  
Published online: November 30, 2022

- [1] A. Splendiani, L. Sun, Y. Zhang, T. Li, J. Kim, C.-Y. Chim, G. Galli, F. Wang, *Nano Lett.* **2010**, *10*, 1271.
- [2] K. F. Mak, C. Lee, J. Hone, J. Shan, T. F. Heinz, *Phys. Rev. Lett.* **2010**, *105*, 136805.
- [3] A. K. Geim, I. V. Grigorieva, *Nature* **2013**, *499*, 419.
- [4] C.-H. Liu, J. Zheng, S. Colburn, T. K. Fryett, Y. Chen, X. Xu, A. Majumdar, *Nano Lett.* **2018**, *18*, 6961.

- [5] R. Verre, D. G. Baranov, B. Munkhbat, J. Cuadra, M. Käll, T. Shegai, *Nat. Nanotechnol.* **2019**, *14*, 679.
- [6] S. Busschaert, R. Reimann, M. Cavigelli, R. Khelifa, A. Jain, L. Novotny, *ACS Photonics* **2020**, *7*, 2482.
- [7] X. Zhang, C. De-Eknamkul, J. Gu, A. L. Boehmke, V. M. Menon, J. Khurgin, E. Cubukcu, *Nat. Nanotechnol.* **2019**, *14*, 844.
- [8] T. D. Green, D. G. Baranov, B. Munkhbat, R. Verre, T. Shegai, M. Käll, *Optica* **2020**, *7*, 680.
- [9] B. Munkhbat, A. B. Yankovich, D. G. Baranov, R. Verre, E. Olsson, T. O. Shegai, *Nat. Commun.* **2020**, *11*, 4604.
- [10] H.-Y. Chang, S. Yang, J. Lee, L. Tao, W.-S. Hwang, D. Jena, N. Lu, D. Akinwande, *ACS Nano* **2013**, *7*, 5446.
- [11] Y. Li, A. Chernikov, X. Zhang, A. Rigosi, H. M. Hill, A. M. Van Der Zande, D. A. Chenet, E.-M. Shih, J. Hone, T. F. Heinz, *Phys. Rev. B* **2014**, *90*, 205422.
- [12] G. A. Ermolaev, Y. V. Stebunov, A. A. Vyshnevyy, D. E. Tatarkin, D. I. Yakubovsky, S. M. Novikov, D. G. Baranov, T. Shegai, A. Y. Nikitin, A. V. Arsenin, V. S. Volkov, *npj 2D Mater. Appl.* **2020**, *4*, 21.
- [13] B. Munkhbat, P. Wróbel, T. J. Antosiewicz, T. O. Shegai, *ACS Photonics* **2022**, *9*, 2398.
- [14] D. Hu, X. Yang, C. Li, R. Liu, Z. Yao, H. Hu, S. N. G. Corder, J. Chen, Z. Sun, M. Liu, Q. Dai, *Nat. Commun.* **2017**, *8*, 1471.
- [15] F. Hu, Y. Luan, M. Scott, J. Yan, D. Mandrus, X. Xu, Z. Fei, *Nat. Photonics* **2017**, *11*, 356.
- [16] V. E. Babicheva, S. Gamage, L. Zhen, S. B. Cronin, V. S. Yakovlev, Y. Abate, *ACS Photonics* **2018**, *5*, 2106.
- [17] G. Ermolaev, D. Grudin, Y. Stebunov, K. Voronin, V. Kravets, J. Duan, A. Mazitov, G. Tselikov, A. Bylinkin, D. Yakubovsky, S. M. Novikov, D. G. Baranov, A. Y. Nikitin, I. A. Kruglov, T. Shegai, P. Alonso-González, A. N. Grigorenko, A. V. Arsenin, K. S. Novoselov, V. S. Volkov, *Nat. Commun.* **2021**, *12*, 854.
- [18] H. Ling, R. Li, A. R. Davoyan, *ACS Photonics* **2021**, *8*, 721.
- [19] H. Ling, J. B. Khurgin, A. R. Davoyan, *arXiv:2204.06067*, **2022**.
- [20] Z. Xu, D. Ferraro, A. Zaltron, N. Galvanetto, A. Martucci, L. Sun, P. Yang, Y. Zhang, Y. Wang, Z. Liu, J. D. Elliott, M. Marsili, L. Dell'Anna, P. Umari, M. Merano, *Commun. Phys.* **2021**, *4*, 215.
- [21] R. Gogna, L. Zhang, H. Deng, *ACS Photonics* **2020**, *7*, 3328.
- [22] F. Wang, C. Wang, A. Chaves, C. Song, G. Zhang, S. Huang, Y. Lei, Q. Xing, L. Mu, Y. Xie, H. Yan, *Nat. Commun.* **2021**, *12*, 5628.
- [23] W. Ma, G. Hu, D. Hu, R. Chen, T. Sun, X. Zhang, Q. Dai, Y. Zeng, A. Alù, C.-W. Qiu, P. Li, *Nature* **2021**, *596*, 362.
- [24] M. Nauman, J. Yan, D. de Ceglia, M. Rahmani, K. Z. Kamali, C. De Angelis, A. E. Miroshnichenko, Y. Lu, D. N. Neshev, *Nat. Commun.* **2021**, *12*, 5597.
- [25] A. A. Popkova, I. M. Antropov, G. I. Tselikov, G. A. Ermolaev, I. Ozerov, R. V. Kirtaev, S. M. Novikov, A. B. Evlyukhin, A. V. Arsenin, V. O. Bessonov, V. S. Volkov, A. A. Fedyanin, *Laser Photonics Rev.* **2022**, *16*, 2100604.
- [26] Y. Song, S. Hu, M.-L. Lin, X. Gan, P.-H. Tan, J. Zhao, *ACS Photonics* **2018**, *5*, 3485.
- [27] J. D. Caldwell, I. Aharonovich, G. Cassabois, J. H. Edgar, B. Gil, D. Basov, *Nat. Rev. Mater.* **2019**, *4*, 552.
- [28] G. Wang, A. Chernikov, M. M. Glazov, T. F. Heinz, X. Marie, T. Amand, B. Urbaszek, *Rev. Mod. Phys.* **2018**, *90*, 021001.
- [29] C. Roxlo, H. W. Deckman, J. Gland, S. Cameron, R. Chianelli, *Science* **1987**, *235*, 1629.
- [30] Z. Wang, G. Yuan, M. Yang, J. Chai, Q. Y. Steve Wu, T. Wang, M. Sebek, D. Wang, L. Wang, S. Wang, D. Chi, G. Adamo, C. Soci, H. Sun, K. Huang, J. Teng, *Nano Lett.* **2020**, *20*, 7964.
- [31] P. G. Zotev, Y. Wang, D. Andres-Penares, T. S. Millard, S. Randerson, X. Hu, L. Sortino, C. Louca, M. Brotons-Gisbert, T. Huq, R. Sapienza, T. F. Krauss, B. Gerardot, A. I. Tartakovskii, *arXiv:2208.06249*, **2022**.
- [32] C. Ma, F. Zhou, P. Huang, M. Li, F. Zhao, Y. Liu, C. Du, X. Li, B.-o. Guan, K. Chen, *Adv. Mater. Technol.* **2022**, 2200432, DOI: <https://doi.org/10.1002/admt.202200432>.

- [33] F. G. De Abajo, *Rev. Mod. Phys.* **2007**, 79, 1267.
- [34] V. E. Babicheva, J. V. Moloney, *Appl. Sci.* **2019**, 9, 2005.
- [35] A. Castellanos-Gomez, M. Buscema, R. Molenaar, V. Singh, L. Janssen, H. S. J. van der Zant, G. A. Steele, *2D Mater.* **2014**, 1, 011002.
- [36] H. Krishnamoorthy, G. Adamo, J. Yin, V. Savinov, N. Zheludev, C. Soci, *Nat. Commun.* **2020**, 11, 1692.
- [37] T. F. Jaramillo, K. P. Jørgensen, J. Bonde, J. H. Nielsen, S. Horch, I. Chorkendorff, *Science* **2007**, 317, 100.
- [38] D. Sarkar, W. Liu, X. Xie, A. C. Anselmo, S. Mitragotri, K. Banerjee, *ACS Nano* **2014**, 8, 3992.
- [39] D. Kong, H. Wang, J. J. Cha, M. Pasta, K. J. Koski, J. Yao, Y. Cui, *Nano Lett.* **2013**, 13, 1341.
- [40] D. Wu, X. Li, L. Luan, X. Wu, W. Li, M. N. Yogeesh, R. Ghosh, Z. Chu, D. Akinwande, Q. Niu, K. Lai, *Proc. Natl. Acad. Sci. U. S. A.* **2016**, 113, 8583.
- [41] D. R. Danielsen, A. Lyksborg-Andersen, K. E. Nielsen, B. S. Jessen, T. J. Booth, M.-H. Doan, Y. Zhou, P. Bøggild, L. Gammelgaard, *ACS Appl. Mater. Interfaces* **2021**, 13, 41886.
- [42] M. Bollinger, J. Lauritsen, K. W. Jacobsen, J. K. Nørskov, S. Helveg, F. Besenbacher, *Phys. Rev. Lett.* **2001**, 87, 196803.
- [43] Y. Li, Z. Zhou, S. Zhang, Z. Chen, *J. Am. Chem. Soc.* **2008**, 130, 16739.
- [44] D. Davelou, G. Kopidakis, G. Kioseoglou, I. N. Remediakis, *Solid State Commun.* **2014**, 192, 42.
- [45] W. Zhou, Z. Yin, Y. Du, X. Huang, Z. Zeng, Z. Fan, H. Liu, J. Wang, H. Zhang, *Small* **2013**, 9, 140.
- [46] X. Yin, Z. Ye, D. A. Chenet, Y. Ye, K. O'Brien, J. C. Hone, X. Zhang, *Science* **2014**, 344, 488.
- [47] J. A. Wilson, A. Yoffe, *Adv. Phys.* **1969**, 18, 193.
- [48] Q. Wang, L. Sun, B. Zhang, C. Chen, X. Shen, W. Lu, *Opt. Express* **2016**, 24, 7151.
- [49] B. Munkhbat, D. G. Baranov, M. Stührenberg, M. Wersäll, A. Bisht, T. Shegai, *ACS Photonics* **2018**, 6, 139.
- [50] J. Joannopoulos, *Photonic Crystals: Molding the Flow of Light*, Princeton University Press, Princeton, NJ **1995**.
- [51] H. Wang, Y.-M. He, T.-H. Chung, H. Hu, Y. Yu, S. Chen, X. Ding, M.-C. Chen, J. Qin, X. Yang, R.-Z. Liu, Z.-C. Duan, J.-P. Li, S. Gerhardt, K. Winkler, J. Jurkat, L.-J. Wang, N. Gregersen, Y.-H. Huo, Q. Dai, S. Yu, S. Höfling, C.-Y. Lu, J.-W. Pan, *Nat. Photonics* **2019**, 13, 770.
- [52] B. Küçüköz, B. Munkhbat, T. O. Shegai, *ACS Photonics* **2022**, 9, 518.
- [53] M. N. Gjerding, M. Pandey, K. S. Thygesen, *Nat. Commun.* **2017**, 8, 15133.